Excerpt from the Proceedings of the 2011 COMSOL Conference in Stuttgart

Modeling of Coupled Fluid Flow and Shear-induced Solidification Kinetics in Rheocasting of Aluminium Alloys

G. Maizza*, and G. Lorenzatto
Dipartimento di Scienza dei Materiali ed Ingegneria Chimica, Politecnico di Torino.
*Corresponding author: C.so Duca degli Abruzzi 24, 10129, Torino, Italy, email: maizza@polito.it

Abstract: The study of semi-solid aluminum and magnesium alloy systems is of scientific and technological importance since they exhibit enhanced castability as well as superior mechanical properties compared to conventional ones owing to their refined microstructure. When a metallic melt undergoes severe shear during solidification a refined microstructure usually results although a quantitative relationship between imposed shear and nucleation density is still obscure.
The present study is inspired by the theoretical work of Schneider and co-workers, who developed a crystallization kinetics to investigate the flow induced crystallization in polymers using an experimentally measured nucleation rate in function of shear stress tensor.
This theory is here adapted to assess its phenomenological suitability in simulating combined temperature- and shear-induced solidification effects in aluminum alloys melts. Essentially, the reference hardware system consists of a cooled rotating stepped shaft and a hot mould containing the liquid metal.
The COMSOL Multiphysics program is invoked to solve the inherent coupled problem involving a set of non linear ordinary differential equations, for aluminum solidification, and the convective momentum and energy transport partial differential equations, for the heat and momentum transport of liquid and semi-solid aluminum. The results are expressed in terms of shear- and thermally-induced solid fractions for a specified angular speed of the shaft.

Keywords: aluminium alloy, semi-solid, solidification kinetics, shear stress effect, rheocasting process.

1. Introduction

Semi-solid processing aims at producing advanced aluminum alloys castings starting from specified fractions of shear-induced solid and liquid [1]. Most of the published papers in modeling and simulation deal with the rheology of semi-solid systems [2] while a minor set of them handle the coupling of liquid transport and solidification kinetics, mainly from an experimental viewpoint. Among the latter, very few take into account for both thermal and shear-induced effects on solidification either experimentally or computationally.
The present work attempts to model the rheocasting process of aluminum alloys by coupling the Schneider and co-workers' crystallization theory with the liquid metal heat transfer and momentum transport partial differential equations. The unique advantage of the proposed theory, which originates from the flow-induced crystallization theory of polymers [3,4], is that it discernes between the nucleation of the solid fraction induced by temperature and that induced by shear.
The rheocasting process may involve during solidification either mechanical or electromagnetic stirring of the melt to attain the desired "semi-solid state". The viscosity of the mushy alloy is a complex function of the formed solid fraction, temperature and shear rate. Beside homogenization of the melt, stirring before casting is found to be effective in the grain refinement of the microstructure [5].
Regardless the stirring method the mushy metal is then injected into a shaped mould to produce the final casting.

2. The Rheocasting Model

The rheocasting process arrangenment is sketched in Fig. 1. It includes a hot isothermal mould, containing the liquid metal, and a rotating cooled stepped shaft. The geometry of the shaft is so selected to maximize the contact area between the cooled rotating shaft and the hot metal. The cooling effect imparted from the cooled rotating shaft to liquid metal is modeled by specifying suitable convective boundary conditions.

As the modeled geometry is axial symmetric only half region is worth of investigation.

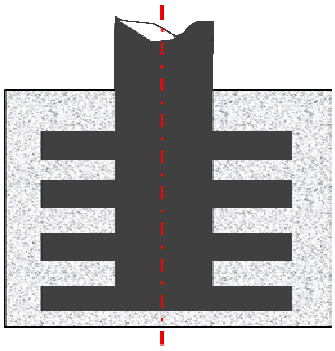

Figure 1. The rheocasting geometry system.

2.1 The Momentum Transport equation: Swirl Flow model

The metal flow in the mould is described by the Navier-Stokes equation:

$$\rho(\mathbf{u}\cdot\nabla)\mathbf{u} = \nabla\cdot[-p\mathbf{I} + \eta(\nabla\mathbf{u} + (\nabla\mathbf{u})^T)] + \mathbf{F} \quad (1)$$

$$\nabla\cdot\mathbf{u} = 0 \quad (2)$$

2.2 The Energy Transport equation: General Heat Transfer model

The temperature change in the liquid system is computed by resorting to the heat-convection equation:

$$\nabla\cdot(-k\nabla T) = \rho C_p\mathbf{u}\cdot\nabla T \quad (3)$$

in which k is thermal conductivity, ρ is density, C_p is heat capacity and **u** is field velocity. The convective term takes into account the heat extracted from the stirring liquid metal by the cooled rotating shaft.

2.3 The Solidification Kinetic Model

According to Schneider and co-workers's theory [3,4] the total solid fraction α formed during cooling and stirring of the liquid metal is a result nucleation and growth induced by two combined effects, i.e, cooling (i.e. thermal) and shear (f). This is mathematically expressed as:

$$\alpha(t) = 1 - \exp\left(-\varphi_0^{\text{global}}(t)\right) \quad (4)$$

where φ_0^{global} is the total volume of crystallized solid, being made of two contributions, i.e.,:

$$\varphi_0^{\text{global}} = \varphi_0^{\text{T}} + \varphi_0^{\text{f}} \quad (5)$$

2.3.1 Temperature-induced solidification kinetics

The total thermally-induced crystallized volume fraction φ_0^T is calculated by the following set of coupled ordinary differential equations (see eqs. 6):

$$\begin{aligned}
&\frac{\partial\varphi_3^T}{\partial t} + \mathbf{u}\cdot\nabla\varphi_3^T = 8\pi\dot{N}^T \qquad (\varphi_3^T = 8\pi N^T)\\
&\frac{\partial\varphi_2^T}{\partial t} + \mathbf{u}\cdot\nabla\varphi_2^T = G_T\varphi_3^T \qquad (\varphi_2^T = 4\pi R_{tot}^T)\\
&\frac{\partial\varphi_1^T}{\partial t} + \mathbf{u}\cdot\nabla\varphi_1^T = G_T\varphi_2^T \qquad (\varphi_1^T = S_{tot}^T)\\
&\frac{\partial\varphi_0^T}{\partial t} + \mathbf{u}\cdot\nabla\varphi_0^T = G_T\varphi_1^T \qquad (\varphi_0^T = V_{tot}^T)
\end{aligned} \quad (6)$$

where G_T is the linear growth rate and N^T is the thermally-induced nucleation density. Thus, it is assumed that both quantities are only function of the local liquid temperature. Their respective formulations will be discussed later.

2.3.2 Shear-induced solidification kinetics

The total shear-induced crystallized volume fraction φ_0^f can be defined analogously to eqs.6, by a set of coupled ordinary differential equations (see eqs. 7):

$$\begin{aligned}
&\frac{\partial\varphi_3^f}{\partial t} + \mathbf{u}\cdot\nabla\varphi_3^f = 8\pi\dot{N}^f \qquad (\varphi_3^f = 8\pi N^f)\\
&\frac{\partial\varphi_2^f}{\partial t} + \mathbf{u}\cdot\nabla\varphi_2^f = G_T\varphi_3^f \qquad (\varphi_2^f = 4\pi R_{tot}^f)\\
&\frac{\partial\varphi_1^f}{\partial t} + \mathbf{u}\cdot\nabla\varphi_1^f = G_T\varphi_2^f \qquad (\varphi_1^f = S_{tot}^f)\\
&\frac{\partial\varphi_0^f}{\partial t} + \mathbf{u}\cdot\nabla\varphi_0^f = G_T\varphi_1^f \qquad (\varphi_0^f = V_{tot}^f)
\end{aligned} \quad (7)$$

where N^f is the nucleation density promoted by the local shear stress, i.e., in a point of the solidifying liquid metal.

3. The Coupling Solution Strategy

As the primary purpose of this work is to test the phenomenological adequacy of the kinetic formalism to model rheocasting of aluminum alloys, a quasi steady-state solution for the liquid transport is preferred, as it is more effective and less time consuming. This approach is indeed advisable at any preliminary setup or design stage of a new rheocasting process hardware. However, a suitable *time* coupling between the solidification kinetics and the quasi-steady state transport model has to be established. This imposes the definition of suitable phenomenological time for the transport model. Note that for more rigorous rheocasting simulations a fully coupled time dependent fluid transport and solidification kinetics is mandatory.
With reference to the arrangement of Fig. 1, we can define an equivalent time as the ratio between the local radius r and the modulus of the local velocity **u**. Thus, the closer is the liquid to the rotating shaft, the faster will be the solidification. Analogously, the larger is the velocity of the liquid in the stirring stage, the faster is the solidification.
The thermal conductivity, heat capacity and density are all functions of the formed solid fraction by the well-known mixture rule:

$$k = \alpha * k^s + (1-\alpha)\cdot k^l \quad (8)$$

$$C_p = \alpha * C_p^s + (1-\alpha)\cdot C_p^l \quad (9)$$

$$\rho = \alpha * \rho^s + (1-\alpha)\cdot \rho^l \quad (10)$$

where the superscripts "l" and "s" denote liquid and solid respectively.
The viscosity of the semi-solid depends on the viscosity of the liquid μ^l and is assumed to be a linear function of temperature:

$$\mu = \mu^l + m_T \cdot T \quad (11)$$

whereas m_T is a constant given in Table 4.

The fundamental Newton's law relates the shear stress τ to the shear rate $\dot{\gamma}$ through the viscosity μ, i.e.,:

$$\tau = \mu \cdot \dot{\gamma} \quad (12)$$

To make the overall rheocasting model computationally fast some further simplifying assumptions are made in the kinetic model outlined in Section 2.
Specifically, the convective terms (i.e the second term in the left hand side of eqs. (6) and (7) can be reasonably neglected [11].
The quasi-steady state trasport model for the liquid metal allows us to consider both nucleation and growth rates as constants. Thus, on integrating with respect to time the set of four kinetic equations reduces to the well-known KJMA-type kinetic equations. This applies for both the temperature- and the shear-induced kinetic model. Accordingly, the resulting solid fraction from the temperature-induced kinetics is:

$$\alpha(t) = 1 - \exp(-K^T(T)\cdot t^4) \quad (13)$$

where K^T is a *gross* rate constant being function of nucleation and growth rates [6]. This gross rate constant is readly determined provided that a set of *time*, *temperature*, *solidification* curves (TTS) are available. These curves are very similar to the *C-shaped* conventional TTT curves and span over the entire solidification range. An example of TTS can be found in reference [7]. Finally, the gross rate constant K^T can be calculated by calculating three constants, namely, a, b, and c [6]. The simple derivation of these three constants takes advantage from the parabolic shape of the TTS curves:

$$K^T(T) = \exp(-a\cdot(T-b)^2 - c) \quad (15)$$

$$a = \frac{n}{(T'-b)^2} ln \frac{t'_{0.5}}{t_0} \quad (16)$$

$$b = T_{nose} \quad (17)$$

$$c = -\ln(\ln(2)/t_0^n) \quad (18)$$

where n, t_0, T', $t'_{0.5}$, T_{nose} are read from the TTS curves [6]. The three constants have to be computed along the 50% solid fraction curve [6].

The TTS curves have to be completed with additional information related to the given alloy. For instance, the equilibrium eutectic temperature of the alloy has to be introduced as upper asymptotic line of the TTS curves. In the bottom of the diagram, another (asymptotic) horizontal line has to be drawn. The region below this line represents the metastable state of a strongly undercooled melt which we assume to be fully solid. The initial temperature of the liquid in the mould can be set to be 100 ºC above the eutectic temperature (i.e. 577 ºC for the selected alloy).

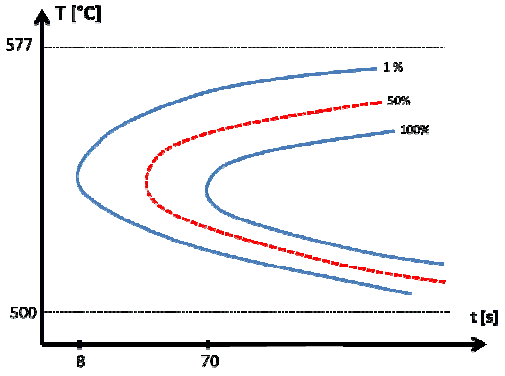

Figure 2. The assumed "C" shaped TTS curves.

The procedure illustrated for the temperature-induced solidification kinetics identically applies to the shear-induced solididification kinetics. In this case, the resulting shear-induced solid fraction is given by:

$$\alpha(t) = 1 - \exp\left(-K^{f}(T,\tau)\cdot t^{3}\right) \qquad (19)$$

As can be seen the main difference between the temperature- and shear-induced kinetics concerns the *gross* rate constants, K^f and K^T, and the time exponents which are 3 and 4 respectively. This implies that the former kinetics is expressed in terms of the nucleation density whereas the latter is expressed in terms of the nucleation rate. However, this choice is not unique, here it is suggested by mere analogy to polymer science. Accordingly, the nucleation density N^f is assumed to be proportional to the shear stress τ:

$$\mathbf{N^{f} = C\cdot abs(\tau)} \qquad (20)$$

where C is a proportionality constant. Also in this case, other authors prefer similar relationship in terms of the nucleation rate [4].

Following Schneider and co-workers' theory, G^T can be assumed to be the same for both temperature- and shear-induced solidification. Using the Umemoto approach [6], the linear growth rate can be expressed by:

$$G^{T} = \beta(T_e - T)^2 \cdot \exp\left(\frac{E}{RT}\right) \qquad (21)$$

in which β is a proportionality constant, T_e is the eutectic temperature, E is the activation energy for the silicon diffusion in the liquid aluminum [9] and R is the gas constant.

To calculate the $K^f(T,\tau)$ in eq.19 the C and β constants have to be found experimentally. For simplicity, we can combine the two constants in a single constant, i.e., $C\cdot\beta^3$ and use only one constant as adjusting kinetic parameter during the simulation of the rheocasting process.

The introduced G^T is defined over the same temperature range of the TTS curves. In Fig. 2, this temperature range corresponds to 577 and 500 ºC.

Finally, two more constraints are introduced to fullfil the TTS curves of the given alloy:

- for temperatures above 577 ºC (+1 ºC), only liquid exists
- for cooling rates above the critical cooling rate, only solid exists.

The critical cooling rate of an alloy system is defined in the same way as to solid state phase transformations. This is given by that cooling curve which is tangent to the nose of the TTS curve at 1% solid fraction.

4. Model Implementation in Comsol Multiphysics

The developed rheocasting employs the "Swirl flow" and the "General heat transfer" applications modes of Comsol Multiphysics 3.5. The following results are computed with a rotational speed of the shaft ω of 0.1 rad/s.

The calculated domain geometry is shown in Fig. 3. The associated boundary conditions are detailed in Table 1 and Table 2, with the help of Fig. 3.

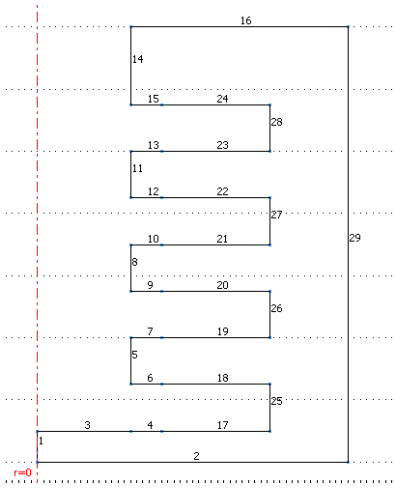

Figure 3. Computational domain and boundary conditions (see Table 1 and 2 for reference).

4.1 Swirl flow boundary conditions

The related boundary conditions are given in Table 1.

Boundary	Type	Condition	Value
1	Symmetry boundary	Axial simmetry	
2;29	Wall	Logarithmic wall function	$\delta_w^+ = 100$
16	Wall	Slip	
3;4;5;6;7;8; 9;10;11;12;13 14;15;17;18;19; 20;21;22;23;24; 25;26;27;28	Wall	Sliding wall	$U_w = 0$ $w_w = \omega r$ $\delta_w^+ = 100$

Table 1. Swirl flow boundary conditions.

4.2 General heat transfer boundary conditions

The convective heat transfer in the liquid phase is enabled in order to couple the heat transfer model to the swirl flow model.
The asscociated boundary conditions are reported in Table 2.

4.3 Domain discretization and solvers

The computational domain is discretized with 13660 triangular elements. Further discretization is performed manually at singular regions, such as the cornes of the stepped shaft.

Boundary	Boundary condition	Value
1	Axial simmetry	
2;16;29	Temperature	$T_0 = 950\ °K$
3;4;5;6;7;8; 9;10;11;12;13 14;15;17;18;19; 20;21;22;23;24; 25;26;27;28	Temperature	$T_0 = 300\ °K$

Table 2. Heat transfer boundary conditions.

The coupled swirl flow and the general heat transfer model is solved using the “stationary segregated” solver and default tolerances and parameters settings except for the temperature field variable which tolerance is set to 0.01 to facilitate the solution convergence.

4.4 Physical Constants

The used general constants are listed in Table 4.

Constant	Value	Ref
ω	0.1 pi [rad/s]	
μ^l	0.0023 [Pa s]	[8]
ρ^l	2460 [kg/(m^3)]	[8]
k^l	90 [W /(m K)]	[10]
k^s	120 [W /(m K)]	[8]
C_p^s	958 [J / (kg K)]	[8]
C_p^l	1054 [J / (kg K)]	[8]
ρ^s	2750 [kg/(m^3)]	[8]
E	136 [kJ / mol]	[9]
m_T	(-1.45 (10^{-4})) [Pa s/K]	
β	54 [mm / (s K^2)]	
C	10^7 [1 / (Pa m^3)]	
R	8.31 [J/(K mol)]	

Table 4. Physical constants.

5. Results and discussion

Figures 4 and 5 demonstrate the basic features of the new solidification kinetic model independently of momentum and energy transport effects. Figures 4 shows the crystalization curves at a local point identified by a constant temperature of 550 ºC and a constant shear of 2.5E-3 Pa. The solid line denotes thermal effect only. The dashed line combines thermal and imposed shear. Figure 5 shows similar crystallization curves for a lower temperature. Figures 4 and 5 clarify the difference in the solidification kinetics when the shear and the thermal effects contribute separately to solidification.

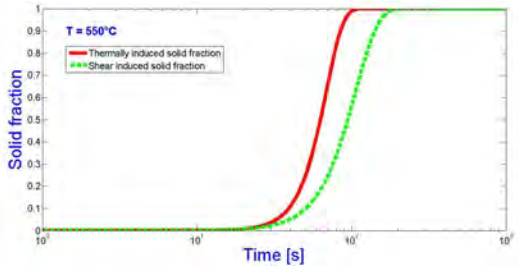

Figure 4. Temperature-induced solid fraction at 550 °C (solid line); combined temperature- and shear- induced solid fraction for a constant shear stress of 2.5e-3 Pa (dashed).

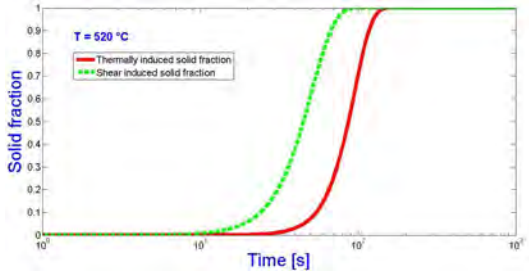

Figure 5. Temperature-induced solid fraction at 520 °C (solid line); combined temperature- and shear- induced solid fraction for a constant shear stress of 2.5e-3 Pa (dashed).

In the following figures the solidification kinetics is solved simultaneously with the transport equations to simulate the overall rheocasting process.

The transport equations are solved in quasi-steady state condition with a constant angular velocity of 0.1 rad/s of the shaft. At each point within the melt the liquid flow and the thermal conditions are related to the solidification kinetics by assuming an equivalent time defined as the ratio of the radius to the local velocity. The solidification at each point is controlled by three basic factors, namely, temperature, equivalent time, and shear stress. The latter, in turn, is function of two more factors, namely, the shear rate and the liquid (or semi-solid) viscosity. Figures 6-8, show the behaviour of these three factors in the liquid/semi-solid region.

Fig. 6 helps identify the region in the melt susceptible of solidification. The solidification range equals to 773-850 K for the assumed alloy.

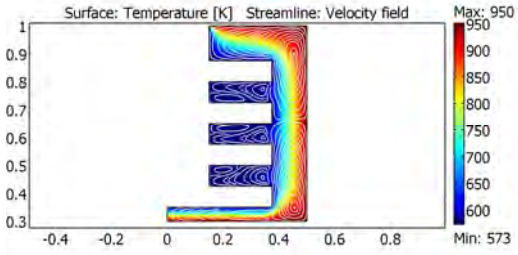

Figure 6. The first controlling factor: temperature.

Figure 7 shows that the equivalent time is larger for larger radii and viceversa. Its maximum value is reached at both the top and the bottom of the mould as expected.

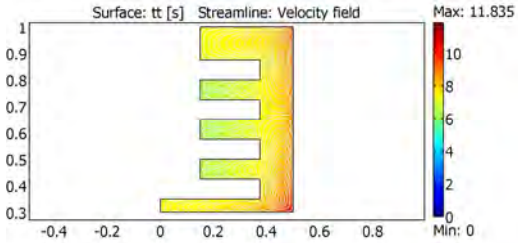

Figure 7. The second controlling factor: equivalent time.

Figure 8 captures the combined effect on the shear stress imparted by the metal viscosity and the shear rate. The former increases as the radius (and incidentally also temperature) decreases. The latter increases as the radius increases. The overall effect is that the absolute value of the shear stress is maximum along the vertical gap existing between the shaft and the mould wall (see also Fig.11) .

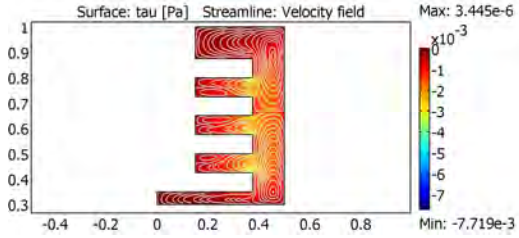

Figure 8. The third controlling factor: shear stress.

In the following Figs. 9-11 the solid fraction separately induced by temperature and shear are compared. The rotating vertical column of the liquid exhibits two large macrocells which touch each other at the mid-height of the mould. Between the four steps of the shaft there exist three liquid regions characterized by minor cells which denote a severe stirring of the liquid metal near the shaft.

The brown region in Fig. 9 represents the solid fraction formed upon rapid cooling (very small equivalent times). As expected, the solid is formed preferentially around the steps of the shaft as a result of the rapid cooling. This solid originates from a melt which has experienced a cooling rate larger than the critical one.

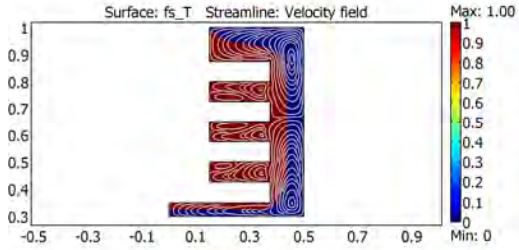

Figure 9. Thermal induced solid fraction.

Figure 10 shows the solid formed for lower cooling rates. This liquid is processed by the implemented kinetics together with the TTS curves. The related thermally induced solidification occurs in a very narrow region. This results from the assumed TTS curves and rotational speed of the shaft.

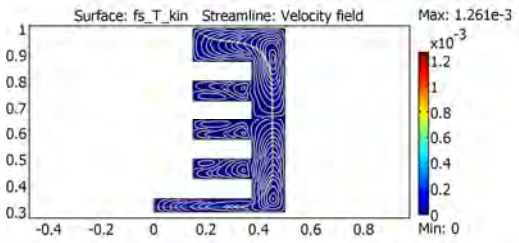

Figure 10. Thermal induced solid fraction (kinetic).

Figure 11 shows the combined temperature- and shear-induced solid fractions with the shear stress field previously shown in Fig. 8. As the equivalent time is very small in this transition region the shear-induced solid fraction is also very small. Larger values of solid fractions would be possible for longer times or larger shear stresses.

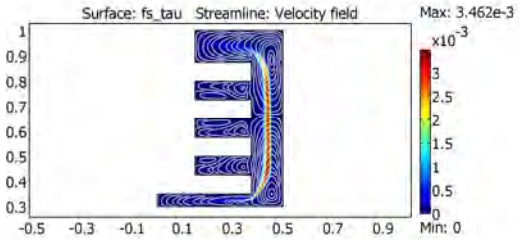

Figure 11. Shear induced solid fraction.

6. Conclusions

A rheocasting model has been successfully developed. It couples the transport equations with a new solidification kinetics which embodies both thermal and shear effects in the melt. Although futher efforts are required to validate the developed model against actual rheocasting experiments, some remarks can be drawn: a) only one kinetic adjusting parameter is required to validate the overall kinetic solidification model; b) the introduced kinetic factors suffice to predict solidification in rheocasting processes. Future progress will concern the development of a fully transient rheocasting model as well as a methodology to build the TTS curves.

7. References

1) Kiuchi M. and Kopp R., Mushy/semi-solid metal forming technology – Present and Future, Annals of the CIRP, 51(2), 653-670, (2002).
2) Lashkari O., and Gomashchi R., *The implication of rheology in semi-solid metal processes: An Overview*, J. Mater. Proc. Tech., 182, 229-240, (2007).
3) Schneider W., Koppl A., J. Berger, *Non-isothermal crystallization: crystallization of polymers: System of rate equations*, Int. Polym. Proc. 3(4) 151-154, (1988).
4) *Modélisation de cristalisation des polymères dans les procédès de plasturgie: quantification des effets thermiques et rhéologiques*, Matthieu Zinet, PhD. Thesis, (2010).
5) Hagayeghi R., Zoqui E. J., Bahai H., *An investigation on the effect of intensive shearing on the grain refinement of A5754 aluminum alloy*, J. Alloy Comp., 481 358-364, (2009).
6) Umemoto M., Horiuchi K., Tamura I., *Pearlite transformation during continuous cooling and its relation to isothermal transformation*, Trans. ISIJ, 23 690-695, (1983).
7) Totten G.E., Mackenzie D.S., Dekker M., *Handbook of Aluminum: alloy production and materials manufacturing*, Kindle Ed., N.Y. (2009).
8) Dijkstra W. O., Vuik C., Katgerman L., *Network model of fluid flow in semi-solid aluminum alloys*, Comp. Mater. Sci., 38 67-74, (2006).
9) Vermolen F. J., Slabbekoorn H.M., van der Zwaag S., *The apparent activation energy for the dissolution of spherical Si-particles in AlSi-alloys*, Mater. Sci. Eng.ng, A231 80-89, (1997).
10) Powell R. W., Ho C. Y., Liley P. E., *Thermal conductivity of selected materials*, Report NSRDS, (1966).
11) Zuidema H., Peters G. W. M., Meijer H. E. H., *Development and validation of a recoverable strain-based model for flow-induced crystallization of polymers*, Macromol. Theory Simul., 10 447-460, (2001).